# NUMERICAL SIMULATIONS OF NON-EQUILIBRIUM TURBULENT BOUNDARY LAYER FLOWING OVER A BUMP

## W. A. El-Askary

*Mechanical Power Engineering Department, Faculty of Engineering,*
*Menoufiya University, Shebin El-Kom, EGYPT*
*Email:* wageeh_elaskary@yahoo.com

## ABSTRACT

Large-eddy simulation (LES) and Reynolds-averaged Navier-Stokes simulations (RANS) with different turbulence models (including the standard $k - \varepsilon$, the standard $k - \omega$, the shear stress transport $k - \omega$ (SST-$k - \omega$ model) and Spalart-Allmaras (S-A)-turbulence models) have been employed to compute the turbulent flow of a two-dimensional turbulent boundary layer over an unswept bump. The predictions of the simulations were compared to available experimental measurements in the literature. The comparisons of the LES and the SST-$k - \omega$ model including the mean flow and turbulence stresses are in satisfied agreements with the available measurements. Though the flow experiences a strong adverse pressure gradient along the rear surface, the boundary layer is unique in that intermittent detachment occurring near the wall. The numerical results indicate that the boundary layer is not followed by mean-flow separation or incipient separation as that shown from the numerical results. The resolved turbulent shear stress is in a reasonable agreement with the experimental data, though the computational result of LES shows that its peak is over-predicted near the trailing edge of the bump, while the other used turbulence models, except the standard $k - \varepsilon$, under-predicts it. Analysis of the numerical results from LES confirms the experimental data, in which the existence of internal layers over the bump surface upstream of the summit and along the downstream flat plate. It also demonstrates that the quasi-step increase in skin friction is due to perturbations in pressure gradient. The surface curvature enhances the near-wall shear production of turbulent stresses and is responsible for the formation of the internal layers.

The present investigation also explains the capability of the used RANS turbulence models to capture the driving mechanism for the surprisingly rapid return to equilibrium boundary layer over the trailing flat plate found in the measurements.

تم في هذا البحث نمذجة سريان إضطرابى للطبقة الجدارية وذلك في وجود عائق سطحي مقـــوس. تـــم اســـتخدام طريقتين مختلفتين للحل وهما RANS, LES باستخدام أربعـــة نمـــاذج إضــــطرابية وهـــي $\varepsilon - K$, $K - \omega$, $SST - K - \omega$, Spalart-Allmaras models وذلك للتنبؤ بخصائص السريان الأضطرابي في الطبقة الجدارية في وجود عائق مقوس على سطح السريان.

في ظل وجود نتائج عملية منشورة تم مقارنة طريقة LES وطريقـــة RANS باســـتخدام نمـــاذج الأضــــطراب المذكورة. أظهرت المقارنات توافق بين LES والنتائج العملية ، كما أوضحت أن أفضل نموذج رياضـــي يمكـــن إستخدامة مع طريقة RANS هو $SST - K - \omega$ في ظل النماذج الأضطرابية المستخدمة. فـــى هـــذا البحـــث أظهرت النتائج النظرية عدم وجود انفصال للطبقة الجدارية بالرغم من وجود تدرج معاكس للضغط على النصف الثاني للسطح المقوس.

فى حالة مقارنة الإجهادات الأضطرابية أوضحت المقارنات أن LES يعطى قيم أعلى بشكل طفيف عـــن النتـــائج العملية وذلك بالقرب من مؤخرة السطح المقوس ولكن نتائج RANS باستخدام نماذج الأضطراب المختلفة أعطت قيم أقل بقليل من النتائج العملية. كما أوضحت نتائج LES وجود طبقة قص داخلية فوق السطح المقوس تبدأ قبـــل قمة السطح المقوس وتمتد حتى فوق السطح الأفقي فيما بعد السطح المقوس فيما يسبب زيادة في قـــيم إجهـــادات الأضطراب.

أظهرت نتائج هذه الدراسة إمكانية استخدام RANS كطريقة بسيطة وغير مكلفة بالرغم من وجود أســـطح غيـــر مستوية يمر عليها السريان في نموذج السريان مما يتسبب في تعقيد سلوك السريان على هذه الأسطح المقوسة.

*Keywords:* Boundary layer; Bump flow; RANS; LES

## 1. INTRODUCTION

The flow past curved surfaces is a complex process which is provoked, in general, by the interaction between geometry- and generated pressure gradients with the boundary layer developing on the surface. In circumstance in which there is a strong pressure, a closed recirculation region may arise following separation. This is the case, for example, in a spanwise uniform, unswept cylinder or surface bump which is confined, in the spanwise direction, by walls that are perpendicular to the cylinder or bump. More generally, the surface of the body interacting with the flow will be highly three-dimensional, and the separation pattern tends to be much more complex, featuring a wide range of topological entities such as curved detachment and attachment lines and nodes, focal points and saddles (Perry and Chong [1]). Moreover, separated regions may be in the form of streamwise-oriented vortical structures which do not reattach and do not form a closed recirculation zone. Examples in which such conditions are encountered are highly-loaded swept wings and fan blades, strongly curved circular ducts and three-dimensional smooth (hill-shaped) constrictions in ducts. Most flows encountered in applications, however, are typically subject to perturbations in external conditions, e.g. pressure gradient and curvature. Generally, when there is a sudden change in the boundary conditions, such as a change in the pressure gradient or surface curvature, the boundary layer responds by forming an internal layer that grows from the wall.

The particular interest of the present study is large-eddy simulation (LES) and Reynolds-averaged Navier-Stokes (RANS) with different turbulence models of the non-equilibrium turbulent boundary layer flowing over a bump. The bump is formed by a prolonged convex surface with two additional short concave regions fore and aft (Figure 1). The flow over the bump permits examination of boundary layer distortion by combined perturbations in streamwise pressure gradient and surface curvature, and recovery following the removal of external perturbations. The particular configuration shown in Figure 1 is considered since boundary layer properties have been reported by Webster et al. [2] and provide a means for evaluation of simulation results. By this geometry, the boundary layer experiences a short concave region, a longer convex region, another short concave region, and then returns to the flat plate. The flow is also subjected to streamwise pressure gradients: first mild adverse, then strong favorable, strong adverse and finally mild favorable, see Webster et al. [2].

LES with dynamic as well as no-subgrid scale modeling was performed by Wu and Squires [3] to calculate the flow of two-dimensional boundary layer

over the bump of Webster et al. [2]. The inflow condition to the bump domain was generated from a separate pre-computed flat plate boundary layer. The same idea is also used in the present research. However, Wu and Squires [3] found great discrepancy occurring in prediction of peak shear stress levels along the rear bump surface.

## 2. COMPUTATIONAL METHOD

### 2.1 Large Eddy Simulation (LES)

In the present work, computation with LES of the incompressible Navier-Stokes equations is employed. Since the large eddies are computed directly, only the effect of the smallest (subgrid) scales of motion is modeled. This should be an advantage in simulation of non-equilibrium boundary layers since, although the large eddies may depend significantly on changes in external conditions and flow history, the small eddies probably respond more rapidly to external perturbations. Therefore, it is still reasonable to model the small scales using simple closures, e.g. eddy viscosity formulations such as the dynamic subgrid-scale (SGS) model of Germano et al. [4], see Wu and Squires [3].

The concept of dynamic modeling is a method for evaluating SGS model coefficients directly from information contained in the resolved turbulent velocity field. The model is formulated to sample turbulent stresses from a band of the smallest resolved scales and then extrapolates this information to the SGS range [4].

The numerical algorithm and solution methods are described here briefly. The spatially filtered incompressible Navier–Stokes equations for resolved scales in LES are

$$\frac{\partial \bar{u}_i}{\partial t} + \frac{\partial}{\partial x_j}\bar{u}_i\bar{u}_j = -\frac{\partial \bar{p}}{\partial x_i} + \frac{1}{Re}\frac{\partial}{\partial x_j}\frac{\partial \bar{u}_i}{\partial x_j} - \frac{\partial \tau_{ij}}{\partial x_j} \qquad (1)$$

$$\frac{\partial \bar{u}_i}{\partial x_i} = 0, \qquad (2)$$

where $\tau_{ij}$ is the subgrid scale (SGS) stress tensor.

All the coordinate variables, velocity components and pressure are non-dimensionalized by the bump cord length $C$, the inflow freestream velocity $U_\infty$ and $\rho U_\infty^2$, respectively. The time is normalized by $C/U_\infty$. The governing equations (1) and (2) are rewritten in a conservative form in generalized coordinates. The dependent variables in the transformed Navier-Stokes equations are volume fluxes across the faces of computational cells, which are equivalent to the use of the contravariant velocity components on a staggered grid multiplied by the Jacobian of the coordinate transformation, see El-Askary et al. [5].

The SGS stress tensor $\tau_{ij}$ is modeled by a Smagorinsky type eddy-viscosity model:

$$\tau_{ij} - \frac{1}{3}\delta_{ij}\tau_{ij} = -2C_s\Delta^2\left|\overline{S}\right|\overline{S}_{ij}. \qquad (3)$$

Where, $C_s$ is the Smagorinisky coefficient and is dynamically computed employing the procedure proposed by Germano *et al.* [4] and $\left|\overline{S}\right| = \sqrt{2\overline{S}_{ij}\overline{S}_{ij}}$ is the resolved-scale strain tensor. In this procedure the eddy kinematic viscosity $\nu_t$ is equivalent to $C_s\Delta^2\left|\overline{S}\right|$ with $\Delta$ as the local grid size. This model is the most commonly used subgrid model in large eddy simulation of incompressible flow as discussed in [6] and successively used by Wu and Squires [3].

The discretization of the convective fluxes in the governing equations is a second-order accurate AUSM formulation [5]. In the AUSM scheme the convective and pressure terms within the inviscid flux vectors are treated separately. The convective terms are approximated upstream biased using a properly defined cell interface velocity, while the pressure term is computed using the sound velocity. The viscous fluxes are discretized using central differences of second-order accuracy. Furthermore, an explicit 5-step Runge-Kutta time stepping scheme of second-order accuracy is used for the temporal integration.

The origin of the streamwise ($x$) coordinate is the onset of curvature, see Figure 1-a. As given in Ref. [2], the bump height reads $h = 20.1mm$ and chord length is $C = 305mm$, i.e., the chord-to-height ratio of the bump is ($C/h = 15.2$). The height of the computational domain is $0.498C$ measured from the flat plate surface ($y = 0$).
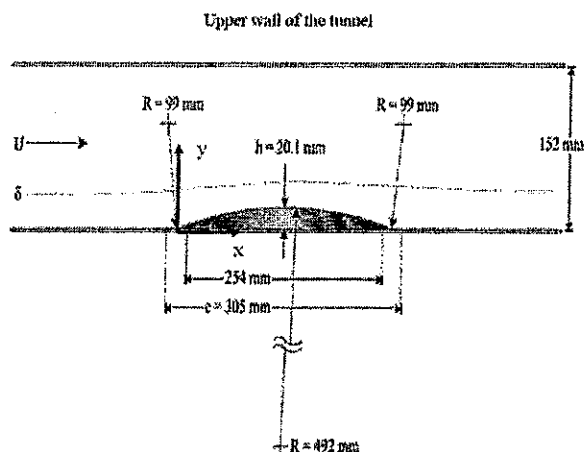
Upper wall of the tunnel



Fig. 1.a Streamwise cross-section of the bump geometry with all dimensions in mm.
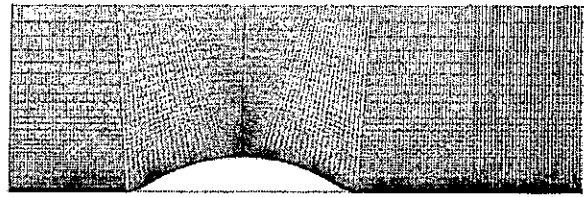


Fig. 1.b The numerical grid used for LES. A view of x-y surface consists of $240 \times 75$ (divided by 2 in x-direction for clear view)

At the surface the no-slip boundary condition, i.e., $u_i = 0$ is imposed. Periodic boundary conditions are applied in the homogeneous spanwise direction of thickness $2.23\delta_o$, where $\delta_o$ is the boundary layer thickness at the inflow of the computational domain. This sufficient spanwise extension was tested and satisfied in [5] and [7]. Dirichlet conditions are applied at the freestream boundary, while a convective boundary condition is considered at the exit plane.

Turbulent inflow conditions for LES must reflect the three-dimensional, unsteady nature of turbulence. In principle, the computational domain should be extended to include all the upstream geometry and flow conditions that may influence flow properties farther downstream. The experimental results of Webster et al. [2] indicated that the bump produces a small distortion of the flow at a location one-third chord length upstream of the onset of curvature ($x/C = -1/3$). In the simulation, it is necessary to specify a realistic, two-dimensional boundary layer at the same location in order to compare LES predictions to experimental measurements. As suggested in [3], in the current study, a time-dependent velocity field at the inflow is generated through a separate LES calculation of flat-plate boundary layer over a momentum-thickness Reynolds number range $1400 \leq Re_\theta \leq 1700$. The flat-plate boundary layer simulation (inflow generator) also requires an inlet boundary condition, which is provided by using the method of Lund and Squires [8]. After a statistically steady state had been reached, all velocity components at a location $Re_\theta = 1500$ are stored for approximately $273\delta_{ref}/U_\infty$ at a time step $\Delta t = 0.01\delta_{ref}/U_\infty$ and are subsequently fed to the inlet ($x/C = -1/3$) of the computational domain of the bump flow simulation. However, the experimental measurements of Webster et al. [2] were collected for three reference momentum thickness Reynolds numbers roughly equal to $Re_\theta = 1500$, 2500 and 4000. The behavior was similar for each case; see Webster et al. [2]. In LES, the lowest Reynolds number is only considered to save the computational

costs and time. The inflow boundary layer thickness was experimentally registered by Webster et al. [2] to be $\delta_{ref}/C = 1.5$ at $x/C = -1/3$. The length of the downstream flat plate is 2/3C and the width of computational domain as discussed previously is $2.23\delta_o$, which corresponds to the value of 0.22C used by Wu and Squires [3]. As case 1 of Wu and Squires [3] for dynamic subgrid scale modeling, the grid generated for the present computation with LES is $240 \times 75 \times 65$ (in streamwise, $x$, normal $y$ and spanwise $z$-direction, respectively), representing freestream constant non-dimensional grid sizes $\Delta x^+$ and $\Delta z^+$ of 44 and 21, respectively, see Figure 1-b. The measured skin friction coefficient $C_f$ of Webster et al. [2] can be used to compute the smallest near-wall grid height $\Delta y$ in the wall normal direction in order to ensure a well resolved boundary layer. According to the definition of the one-wall unit, i.e., $\Delta y^+ = 1$, the first cell height at the wall is computed from

$$\Delta y = \frac{y^+ \nu}{\sqrt{\tau_w/\rho}} = \frac{y^+ \nu}{U_\infty \sqrt{C_f/2}} \cdot$$

An expansion factor of 1.1 is used to generate the grid in the wall-normal direction.

## 2.2 Reynolds-Averaged Navier-Stokes (RANS)

In the family of RANS, the eddy viscosity turbulence models is based on the assumption that the Reynolds stress tensor $\tau_{ij}$ is related to the mean strain rate through an apparent turbulent viscosity called eddy viscosity $\nu_t$

$$\tau_{ij} = \nu_t \overline{S}_{ij} = \nu_t (\frac{\partial \overline{u}_i}{\partial x_j} + \frac{\partial \overline{u}_j}{\partial x_i}) \tag{4}$$

In all RANS models, the eddy viscosity is computed through partial differential equations, either two-equation model, such as $k-\varepsilon$ of Launder and Spalding [9], $k-\omega$ of Wilcox [10] and shear stress transport $k-\omega$, (SST-model of Menter [11]) or one equation turbulence model of Spalart and Allmaras [12] (SA-model). The equations of the mentioned turbulence models used here are given in references [9-12]. Detailed derivation of turbulence models can be also found in references, such as Launder and Spalding [9], Yakhot and Orszag [13], Shih et al. [14] and Wilcox [10].

### 2.2.1 The standard $k-\varepsilon$ model

The standard $k-\varepsilon$ model was derived by assuming that the flow is fully turbulent and the effects of molecular viscosity are negligible, Launder and Spalding [9]. The turbulent kinematic viscosity is computed from turbulent kinetic energy k and its dissipation rate $\varepsilon$ as follows:

$$\nu_t = C_\mu \frac{k^2}{\varepsilon} \tag{5}$$

$$\frac{\partial}{\partial x_j}(u_j k) = \frac{\partial}{\partial x_j}\left[\left(\nu + \frac{\nu_t}{\sigma_k}\right)\frac{\partial k}{\partial x_j}\right] + P_k - \varepsilon \tag{6}$$

where the turbulent production rate is defined as

$$P_k = 2\nu_t S_{ij} S_{ij} \tag{7}$$

The transport equation for the kinetic energy dissipation $\varepsilon$ is given in the form of

$$\frac{\partial}{\partial x_j}(u_j \varepsilon) = \frac{\partial}{\partial x_j}\left[\left(\nu + \frac{\nu_t}{\sigma_\varepsilon}\right)\frac{\partial \varepsilon}{\partial x_j}\right] + (c_{\varepsilon 1} P_k - c_{\varepsilon 2}\varepsilon)\frac{\varepsilon}{k} \tag{8}$$

The empirical values of constants appearing in the transport equations are given in Table 1.

**Table 1.** Constants of the standard $k-\varepsilon$ model

| $c_{\varepsilon 1}$ | $c_{\varepsilon 2}$ | $C_\mu$ | $\sigma_k$ | $\sigma_\varepsilon$ |
|---|---|---|---|---|
| 1.44 | 1.92 | 0.09 | 1.0 | 1.3 |

### 2.2.2 The original $k-\omega$ model

The second turbulence model developed by Wilcox [10] is $k-\omega$ model. In addition to the k equation a new equation is specified for the specific dissipation rate ω to determine the turbulent viscosity

$$\frac{\partial}{\partial x_j}(u_j k) = \frac{\partial}{\partial x_j}\left[(\nu + \sigma_{k1}\nu_t)\frac{\partial k}{\partial x_j}\right] + P_k - Y_k \tag{9}$$

$$\frac{\partial}{\partial x_j}(u_j \omega) = \frac{\partial}{\partial x_j}\left[(\nu + \sigma_{\omega 1}\nu_t)\frac{\partial \omega}{\partial x_j}\right] + P_\omega - Y_\omega \tag{10}$$

The turbulent viscosity $\mu_t$ is computed by combining $k$ and $\omega$ as follows:

$$\mu_t = \alpha^* \frac{\rho k}{\omega} \tag{11}$$

The production of the specific dissipation rate $P_\omega$ is defined from

$$P_\omega = \alpha \frac{\omega}{k} P_k \tag{12}$$

The closure coefficients $\alpha$ and $\alpha^*$ are taken to be unity, see Ref. [10].

The dissipation of k is represented by

$$Y_k = \beta^* f_{\beta^*} k\omega \tag{13}$$

with

$$f_{\beta^*} = \begin{cases} 1 & \chi_k \le 0 \\ \dfrac{1+680\chi_k^2}{1+400\chi_k^2} & \chi_k > 0 \end{cases} \qquad (14)$$

where, $\chi_k \equiv \dfrac{1}{\omega^3}\dfrac{\partial k}{\partial x_j}\dfrac{\partial \omega}{\partial x_j}$, $\beta^* = \beta_\infty^* \left(\dfrac{4/15+(\mathrm{Re}_t/R_\beta)^4}{1+(\mathrm{Re}_t/R_\beta)^4}\right)$

and $\mathrm{Re}_t = \dfrac{\rho k}{\mu \omega}$.

The dissipation of $\omega$ is given by

$$Y_\omega = \beta f_\beta \omega^2 \qquad (15)$$

where,

$$f_\beta = \dfrac{1+70\chi_\omega}{1+80\chi_\omega}, \qquad (16)$$

$$\chi_\omega = \left|\dfrac{\Omega_{ij}\Omega_{jk}\sqrt{\dfrac{P_k}{2\mu_t}}}{(\beta_\infty^*\omega)^3}\right| \qquad (17)$$

and

$$\Omega_{ij} = \dfrac{1}{2}\left(\dfrac{\partial u_i}{\partial x_j} - \dfrac{\partial u_j}{\partial x_i}\right) \qquad (18)$$

The model constants are $\beta_\infty^* = 0.09$, $\beta = 0.072$, $R_\beta = 8$, $\sigma_k = 0.5$ and $\sigma_\omega = 0.5$.

At a no-slip wall, all turbulent quantities, except $\omega$ are set to zero. As pointed out by Wilcox [10], $\omega$ satisfies the following equation near the wall:

$$\omega \to \dfrac{6}{\beta_1 y^2} \quad \text{as} \quad y \to 0.$$

### 2.2.3 The shear-stress transport (SST) $k-\omega$ model

The basic idea behind the SST model is to retain the robust and accurate formulation of the Wilcox $k-\omega$ model in the near wall region, and to take advantage of the freestream independence of the $k-\varepsilon$ model in the outer part of the boundary layer. In order to achieve this goal, the $k-\varepsilon$ model is transformed into a $k-\omega$ formulation, see Menter [11]. The original model is multiplied by a function $F_1$ and the transformed model by a function $1-F_1$ and both are added together. The function $F_1$ will be designed to be one in the near wall region (activating the original model) and zero away from the surface. The final form is

$$\dfrac{\partial}{\partial x_j}(u_j k) = \dfrac{\partial}{\partial x_j}\left[(\nu + \sigma_{k1}\nu_t)\dfrac{\partial k}{\partial x_j}\right] + P_k - Y_k \qquad (19)$$

$$\dfrac{\partial}{\partial x_j}(u_j \omega) = \dfrac{\partial}{\partial x_j}\left[(\nu + \sigma_{\omega1}\nu_t)\dfrac{\partial \omega}{\partial x_j}\right] + \gamma P_\omega$$
$$- Y_\omega + 2(1-F_1)\sigma_{\omega2}\dfrac{\nu_t}{k}\dfrac{\partial k}{\partial x_j}\dfrac{\partial \omega}{\partial x_j} \qquad (20)$$

Let $\phi$ represents new model constant that can be calculated from the constants $\phi_1(\sigma_{k1},\sigma_{\omega1},\beta_1)$, and $\phi_2(\sigma_{k2},\sigma_{\omega2},\beta_2)$ as follows

$$\phi = F_1\phi_1 + (1-F_1)\phi_2 \qquad (21)$$

with

$\sigma_{k1} = 0.85, \sigma_{\omega1} = 0.65, \beta_1 = 0.075,$

$\beta^* = 0.09, \kappa = 0.41, \gamma_1 = \beta_1/\beta^* - \sigma_{\omega1}\kappa^2/\sqrt{\beta^*}$

and

$\sigma_{k2} = 1.0, \sigma_{\omega2} = 0.856, \beta_2 = 0.0828,$

$\beta^* = 0.09, \kappa = 0.41, \gamma_2 = \beta_2/\beta^* - \sigma_{\omega2}\kappa^2/\sqrt{\beta^*}$

The function $F_1$ is defined as follows:

$$F_1 = \tanh(\arg_1^4) \qquad (22)$$

with

$$\arg_1 = \max\left(\min\left(\dfrac{\sqrt{k}}{0.09\omega y}; 0.45\dfrac{\omega}{\Omega}\right); \dfrac{400\nu}{y^2\omega}\right) \qquad (23)$$

where $y$ is the distance to the next surface and the eddy-viscosity is defined as:

$$\nu_t = \dfrac{a_1 k}{\max(a_1\omega; \Omega F_2)} \qquad (24)$$

where $a_1 = 0.3$ and $\Omega$ is the absolute value of the vorticity. $F_2$ is given by:

$$F_2 = \tanh(\arg_2^2) \qquad (25)$$

with:

$$\arg_2 = \max\left(2\dfrac{\sqrt{k}}{0.09\omega y}; \dfrac{400\nu}{y^2\omega}\right) \qquad (26)$$

In the SST model, Menter [11] suggested the use of the following near-wall value: $\omega \to 10\dfrac{6}{\beta_1 y^2}$ as $y \to 0$.

### 2.2.4 Spalart-Allmaras model (SA-model)

The Spalart-Allmaras one-equation model [12] proved to be very efficient and robust for various challenging aerodynamic flows and was already successfully applied to many different calculations with the presence of pressure gradient. In the SA-model, the eddy viscosity is computed through a partial differential equation. In particular the eddy viscosity $\nu_t$ is computed by an intermediate variable $\widetilde{\nu}$ through the relation:

$$v_t = \tilde{v} f_{v1}(\chi), \tag{27}$$

where $\chi$ is the ratio

$$\chi = \frac{\tilde{v}}{v} \tag{28}$$

and $f_{v1}$ is a damping function. The intermediate variable $\tilde{v}$ is computed by solving a differential equation that can be written in compact form as:

$$\frac{\partial(u\tilde{v})}{\partial x} + \frac{\partial(v\tilde{v})}{\partial y} = \frac{\partial}{\partial x}\left[\frac{(v+\tilde{v})}{\sigma}\frac{\partial \tilde{v}}{\partial x}\right] + \frac{\partial}{\partial y}\left[\frac{(v+\tilde{v})}{\sigma}\frac{\partial \tilde{v}}{\partial y}\right] \tag{29}$$

$$+ C_{b1}(1-f_{t2})\tilde{S}\tilde{v} - (C_w f_w - C_b f_{t2}/\kappa^2)(\tilde{v}/d)^2 + f_{t1}\Delta u^2$$

where, $f_{v1} = \chi^3/(\chi^3 + C_{v1}{}^3)$, $\chi = \tilde{v}/v$ and $v$ is the laminar kinematic viscosity.

The production term $\tilde{S}$ is given by:

$$\tilde{S} = S + (\tilde{v}/\kappa^2 d^2)f_{v2} \tag{30}$$

S is the magnitude of the vorticity, d is the distance to the wall; and

$$f_{v2} = 1 - \chi/(1+\chi f_{v1}) \tag{31}$$

The destruction function, $f_w$, is given by

$$f_w = g\left(\frac{1+C_{w3}{}^6}{g^6 + C_{w3}{}^6}\right)^{1/6} \tag{32}$$

where, $g = r + C_{w2}(r^6 - r)$ and $r = \tilde{v}/(\tilde{S}\kappa^2 d^2)$.

$$f_{t1} = C_{t1}g_t \exp(-C_{t2}(\omega_t^2/\Delta u^2)(d^2 + g_t^2 d^2)) \tag{33}$$

The transition functions are

$$f_{t2} = C_{t3}\exp(-C_{t4}\chi^2) \tag{34}$$

where, $g_t = \min(0.1, \Delta u/\omega_t \Delta x)$.

In the transition functions, $\omega_t$ is the vorticity at the surface and $\Delta x$ is the grid spacing along the $x$ direction. The velocity difference between a field point and the surface was $\Delta u$.

Spalart and Allmaras [12] used the following set of empirical constants:

$C_{b1} = 0.1355, C_{b2} = 0.662, \sigma = 2/3, \kappa = 0.41,$

$C_{w1} = C_{b1}/\kappa^2 + (1+C_{b2})/\sigma, C_{w2} = 0.3, C_{w3} = 2,$

$C_{v1} = 7.1, C_{t1} = 1, C_{t2} = 2, C_{t3} = 1, C_{t4} = 2.$

The inflow boundary condition of $\tilde{v}$ is $\tilde{v} = 0.1v$ and taken to be zero at the wall.

The model doesn't include the turbulent kinetic energy k, which is simply dropped from the averaged equations [12]. This missing feature doesn't seem to play a decisive role in the computations presented in the original paper. Since the transition tripping functions introduced by Spalart and Allmaras [12] are rarely implemented by researchers [15] due to

numerical and implementation difficulties, they are dropped in the present work.

All computations of RANS are based on a finite volume numerical method for solving two-dimensional Reynolds-averaged Navier–Stokes equations. The well-known SIMPLE algorithm was applied for coupling the velocity and pressure fields. More details about the numerical scheme are given in [9, 16-17]. In this method, a non-uniform staggered grid arrangement in which the velocity components are located on the control volume surfaces and the scalar quantities are located inside the control volumes. For the computation of fluxes, the power-law differencing scheme of Patankar [18] was used. With the differencing scheme, the resulting matrix of coefficients is diagonally dominant; therefore, the scheme is unconditionally stable. The *discretized* algebraic equations were solved using a line-by-line method with appropriate under-relaxation factors for faster convergence.

The two-dimensional RANS *computational* domain has the same streamwise length of LES domain, but its height (H) represents the original tunnel height of the experimental test rig of Webster et al. [2], in which H/C=0.498. The grid used for RANS is $240 \times 100$ in streamwise and wall-normal direction, respectively. It is clear that, the number of grid points for RANS in y direction is more than that of LES, because RANS simulation considers the two walls of the wind tunnel with near-wall fine grid spacing of order $y^+ = 1$.

## 3. NEAR WALL TREATMENTS OF RANS

In the region near the walls (the upper and lower walls), the gradient of quantities is considerably high and requires fine grids close to the wall to capture the change of quantities. This causes the calculation to become more expensive meaning time-consuming, requiring greater memory and faster processing on the computer, as well as expensive in terms of complexity of equations. For $k - \varepsilon$ turbulence model, a wall function which is a collection of semi-empirical formulas and functions provides a cheaper calculation by substituting the fine grids with a set of equations linking the solutions' variables at the near-wall cells and the corresponding quantities on the wall. For mild curved flows where no separation flow occurs, the standard wall function proposed by Launder and Spalding [9] becomes reliable. For the $k - \omega$ models, when the low-Reynolds number effects are activated, the near-wall grids have to be very fine to obtain the better results for the near wall modeling. However, for the high-Reynolds number flows which are of concern here, the low-Reynolds number effects can be neglected so that the near wall grids follow a rule of the wall function. The near wall

treatment of SA-model is considered as explained in Ref. [12].

To generate a suitable inflow condition to the considered computational domain of RANS simulation, a duct of one meter length and the same height of the computational domain is first simulated and then the results are extracted to feed the inflow data to the bump domain. The grid sizes ($\Delta x, \Delta y$) of the duct is the same as that of the upstream portion of the bump. Uniform velocity to the duct with $U_{bulk} = 15.5 m/s$, which is corresponding to $U_{\infty}$ of the experimental work of Ref. [2] (nearly 16.6 m/s). The inflow turbulence intensity is considered to be 0.2% as reported in [2]. For the $k - \varepsilon$ model, the dissipation rate of $k$ at the inlet of the duct is computed from $\varepsilon = C_{\mu}^{0.75} \dfrac{k^{1.5}}{0.07 D_{H}}$, where $C_{\mu}$ is constant and it is approximately equal to 0.09 and $D_{H}$ is the duct hydraulic diameter. The same value of turbulence kinetic energy is specified for the $k - \omega$ model, and $\omega$ is presumed as $\omega = \dfrac{\sqrt{k}}{0.07 D_{H} C_{\mu}^{0.25}}$.

## 4. RESULTS AND DISCUSSIONS

Computations with different methods including LES and RANS simulations with different turbulence models were performed. The simulations verifications are based on the experimental measurements presented in Ref. [2].

Gross features of the turbulent boundary layer structure on the bump surface are visualized using the iso-vorticity contours and are shown in Figure 2. Incoming turbulent boundary layer (from left to right) with its fingerlike forms over the upstream flat plate is noticed. The inclination angle of the finger forms is strongly affected by the presence of the bump surface, in which a strong increase of the structure angle is clearly visible near the top of the bump surface, because of the increase of momentum convection normal to the wall towards the outer layer and the presence of a strong pressure gradient (discussed later). However, after the trailing edge of the bump (in the downstream flat surface), the perturbations produced by the bump surface are still observed in the relaxation of the vortices with high inclination angles to the surface.

Figure 3 shows the unsteady streamwise velocity contours computed by LES. The ejection-sweeping mechanism of the turbulent boundary layer is noticed. Approaching the top of the bump surface, it is clearly seen a near wall internal shear layer generation, which extends in the downstream of the bump surface. A strong elongation of near-wall

eddies with lowering the near-wall velocity with the presence of strong pressure gradient on the rear half of the bump is also observed.



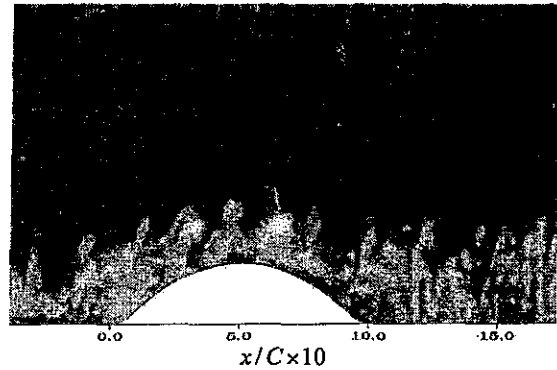Figure 2. Iso-voricity contours near the bump surface



$x / C \times 10$

Figure 3. Unsteady velocity contours on the bump surface

Figure 4 shows comparisons of the mean non-dimensionalized surface pressure coefficients $C_p$ with the experimental data of Webster et al. [2]. The static pressure distribution is non-dimensionalized by the freestream dynamic pressure ($P_{\infty} = 0.5 \rho U_{ref}^2$) at the upstream reference location ($x/C = -0.33$: $C_p = P_w / P_{\infty} = (P - P_{ref})/0.5 \rho U_{ref}^2$).

As discussed in the introduction, the flow encountered a mild adverse pressure gradient as it approached the bump. The flow accelerated in a strong favorable pressure gradient on the upstream side of the bump and then decelerated in the similarly strong adverse pressure gradient on the downstream side. Downstream of the bump was a constant-area rectangular section and the flow relaxed back to a near-zero pressure gradient. All the numerical simulations, including the present LES and the different RANS models, agree reasonably with the experimental measurements of Webster et al. [2] in representing the bump surface pressure distribution.

The upper wall pressure distribution is numerically introduced in Figure 5. There aren't available experimental measurements on the upper wall of the tunnel, so only the RANS results with all tested turbulence models are presented. The reduction of pressure to its lowest value is corresponding to the

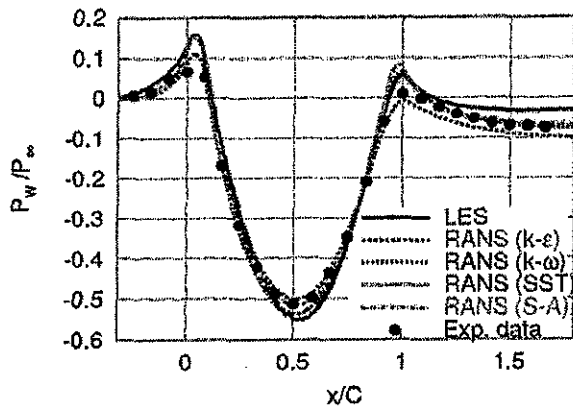reduction of flow cross section due the presence of the bump wall.



**Figure 4.** Wall-static pressure coefficient on the bump surface compared with that measured by Webster et al. [2]
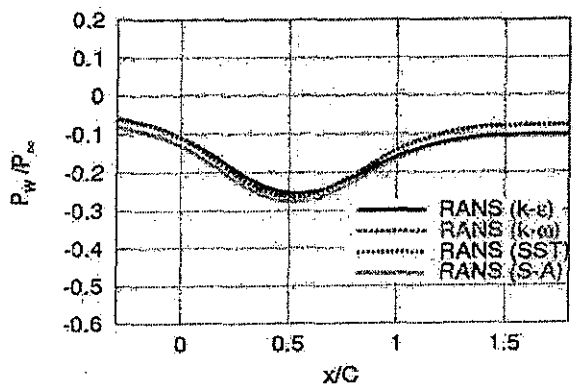


**Figure 5.** Wall-static pressure coefficient on the upper wall of the tunnel

The skin friction coefficient is defined as: $C_f = \tau_w / 0.5\rho U_{ref}^2$, where $\tau_w$ is the local wall-shear stress as shown in Figure 6. The skin-friction coefficient exhibits an interesting response to the combined perturbations in pressure gradient and curvature. It is clear that, the skin-friction coefficient tends to decrease when a boundary layer is subjected to adverse pressure gradient or convex wall; favorable pressure gradient or concave wall tends to increase the skin-friction coefficient. The slight dip centre near the bump apex ($x/C = 0.5$) was clearly evident in the experimental data of Webster et al. [2] and the present simulation with LES and not predicted with all RANS models. However, the numerical results obtained from $k - \omega$, SST $k - \omega$ and SA turbulence models are fairly good, but the standard $k - \varepsilon$ produces higher values of $C_f$. The presence of streamline curvature of flow is the main cause of the over-prediction produced in the results of the standard $k - \varepsilon$ model. An incipient separation is numerically predicted near the bump rear with LES

and all RANS models except the standard $k - \varepsilon$ model. However, there is not sufficient resolution of the experimentl data to show any incipient separation.
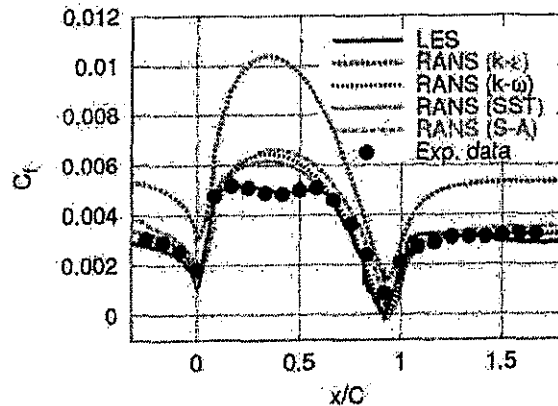


**Figure 6.** Wall-skin friction coefficient on the bump surface compared with that measured by Webster et al. [2]

The inverse criterion of the upper-wall pressure distribution (shown in Figure 5) is observed in the upper-wall skin friction coefficient as seen in Figure 7. The low pressure near the bump apex is responsible for the increase in $C_f$ at this location on the upper wall.

The streamwise mean velocity profiles at eight streamwise locations, reading $x/C = 1/2, 2/3, 5/6$, $11/12, 1, 7/6, 4/3$ and $5/3$, are compared with the experimental measurements of Webster et al. [2] and shown in semi-logarithmic form in Figure 8. The velocity profiles are normalized by the local external free-stream velocity $U_\infty$ and the vertical coordinate is normalized by the inflow momentum thickness, $\theta_{ref} = C/78$.
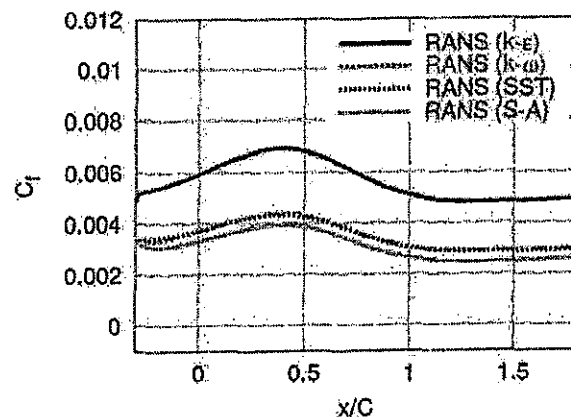


**Figure 7.** Wall-skin friction coefficient on the upper wall of the tunnel
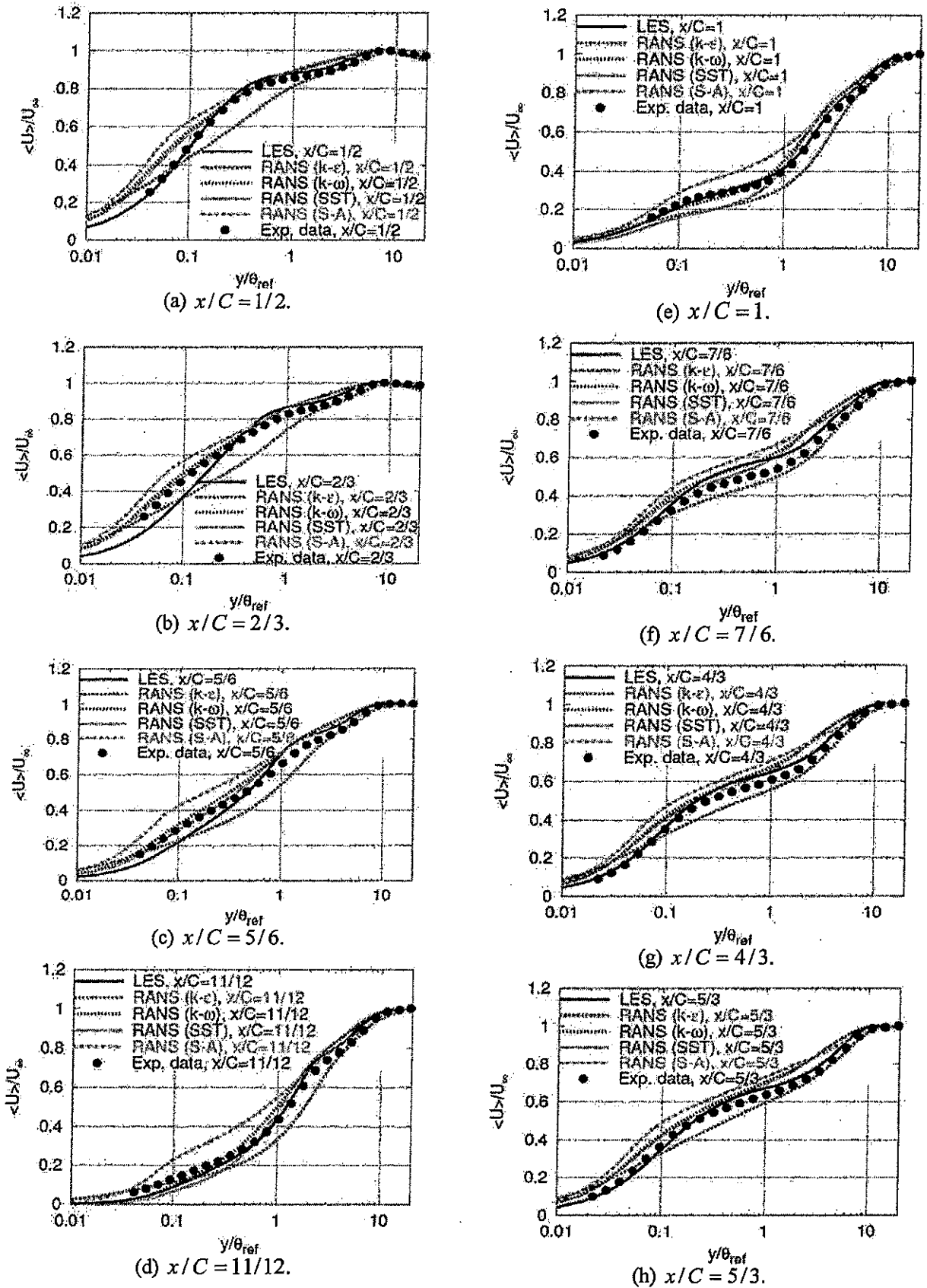
Figure 8. Predicted mean-streamwise velocity against that measured by Webster et al. [2].

The predicted mean streamwise velocity profiles using LES and RANS with $k-\omega$ and SST $k-\omega$ turbulence models at all locations given above are in reasonably good agreement with the measurements of Webster et al. [2]. The presence of streamline curvature strongly affects the performance of the standard $k-\varepsilon$ as well as the S-A turbulence models. The LES results exhibit exceptions at near-surface region along $x/C = 2/3$ and $5/6$. At these locations, a shear layer may be start to develop from the surface and consequently strong intermittent reversal of the boundary layer. Over the downstream flat plate, LES and RANS with $k-\omega$ and SST $k-\omega$ turbulence models predictions compare reasonably well with measurements and show a rapid relaxation to the same of flat plate boundary layer. However, the standard $k-\varepsilon$ turbulence model exhibits a measurable under-predictions at all stations compared to those from the other simulations in the logarithmic region at the same time of the over-predictions of the S-A model. Near the trailing edge of the bump, i.e., in the concave wall region, the SST $k-\omega$ turbulence model is going to under-predict the experimental data in the logarithmic region. Figure 8-a. shows that for $y/\theta_{ref} > 1.0$, the velocity profiles of all turbulence models and LES are well collapsed with the experimental data of Ref. [2]. Generally, as noticed from Figures 8-b to 8-h, the SST $k-\omega$ turbulence model is approaching to the experimental results giving the best turbulence model in view of the other used RANS turbulence models in the present research.

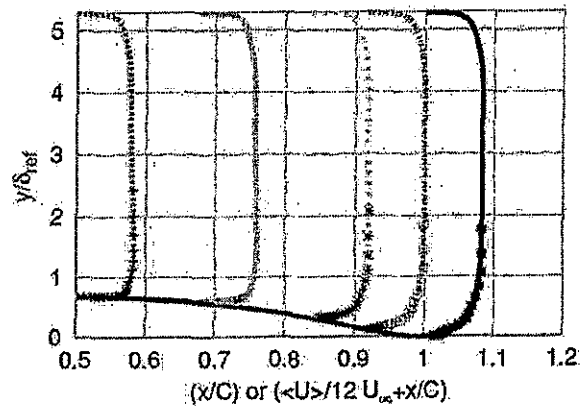The predicted mean streamwise velocity using SST $k-\omega$ turbulence model against that measured by Webster et al. [2] in the entire domain from the bump surface to the upper wall of the duct at the locations $x/C = 1/2, 2/3, 5/6, 11/12$ and 1 is shown in Figure 9. Clearly visible is the good performance of the SST $k-\omega$ turbulence model. It is noticed also an asymmetric development of the velocity profiles on the two walls. On the bump wall the boundary layer thickness is greatly increased with approaching the trailing edge of the bump because of the strong adverse pressure gradient generated on the downstream half of the bump, while the small adverse pressure gradient on the upper wall causes lower increasing rate of the boundary layer thickness.

The turbulent stresses can be computed from the estimated mean strain rate as $<u'_i u'_j> = \dfrac{2}{3}\dfrac{k}{\rho}\delta_{ij} - 2\mu_t \bar{S}_{ij}$, where $k$ is the turbulent kinetic energy and $\mu_t$ is the turbulent viscosity.



**Figure 9.** Predicted mean- streamwise velocity using SST $k-\omega$ turbulence model against that measured by Webster et al. [2] in the entire domain from the bump surface to the upper wall of the duct at the locations $x/C = 1/2, 2/3, 5/6, 11/12$ and 1 (from left to right).

The predicted profiles of streamwise turbulent stress, $<u'u'>$, are compared with the experimental measurements and shown in Figure 10. At the downstream previous mentioned locations reading: $(x/C = 1/2, 2/3, 5/6, 11/12, 1, 7/6, 4/3$, and $5/3)$, shown in Figure 10-a to 10-h, the numerical results of LES as well as RANS with the given turbulence models are presented. The one-equation model of Spalart-Allmaras (S-A model) is not illustrated here, because there is no explicit equation from which the turbulence kinetic energy can be computed. The standard $k-\varepsilon$ turbulence model produces good verification at all locations in the outer layer of the turbulent boundary layer in view of the other considered RANS models. Good predictions of the near wall peaks of the turbulence stress at all locations can be fairly good predicted by LES, while qualitative results from RANS models are seen. At the bump apex $(x/C = 1/2$, see Figure 10-a), the profile has a knee point at approximately $y/\theta = 1$ as registered by Webster et al. [2] and the same knee can be observed in the present numerical results approximately at the same height. This results from the destruction of turbulence production in the outer layer by convex curvature and favorable pressure gradient and the development of an internal layer over the upstream convex surface. In the profiles on the downstream side of the bump, the knee point and the location of the local maximum moves away from the wall, indicating that the internal layer grows away from the wall in the adverse pressure gradient.
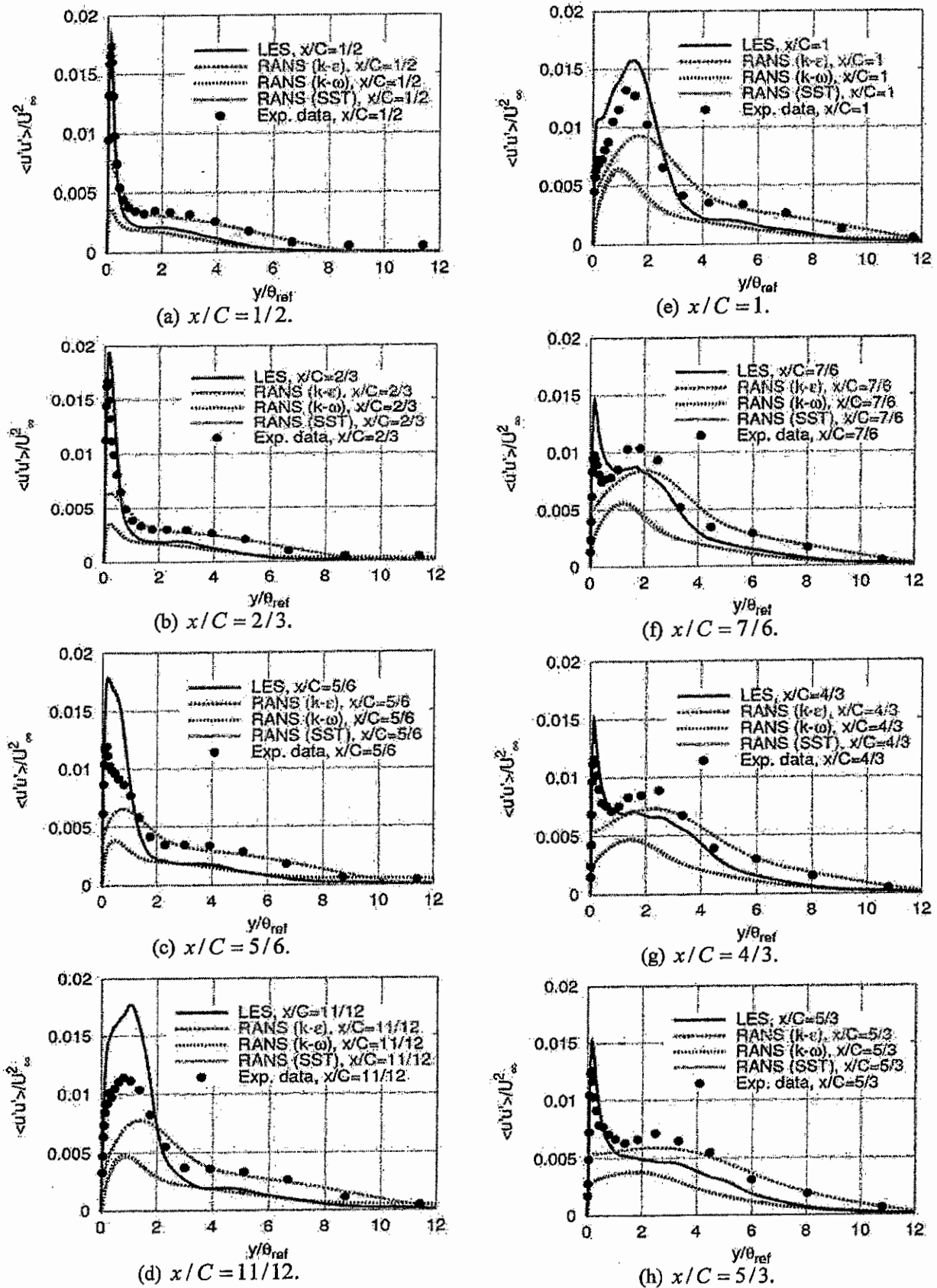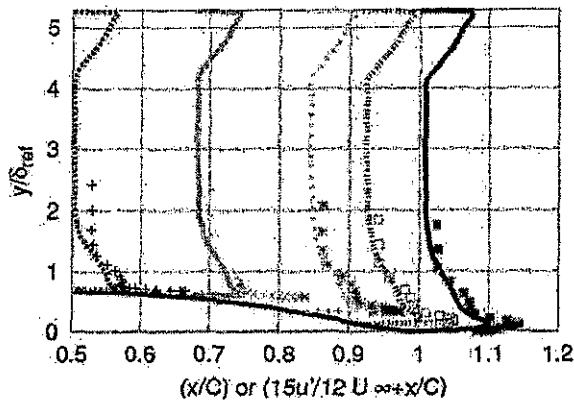
**Figure 10.** Predicted mean-streamwise turbulent stress against that measured by Webster et al. [2].

By the $x/C = 1$ location as shown in Figure 10-e, the internal layer had grown approximately to $y/\theta = 3$ in the experiment of Webster et al. [2] and the same is observed qualitatively in RANS with $k - \omega$ and SST $k - \omega$ turbulence models, while it is delayed to $y/\theta = 4$ in the LES results. At this location the boundary layer thickness had also grown significantly.

The flow encountered a second internal layer, which appears explicitly at $x/C = 7/6$, as seen in Figure 10-f, where two local maxima in the streamwise turbulent normal stress profile are experimentally and numerically with the present LES only observed, while non of the present RANS models can predict this behavior. The inner peak is due to the new internal layer and the outer peak is the remnants of the upstream internal layer. As the flow evolves downstream on the flat plate, the new internal layer grows while the outer peak decays away.

Using SST $k - \omega$ turbulence model, the square root of the streamwise turbulent normal stress is presented against that measured by Webster et al. [2] in the entire domain from the bump surface to the upper wall of the duct at the locations $x/C = 1/2, 2/3, 5/6, 11/12$ and 1 is shown in Figure 11. Fairly good verification of the SST $k - \omega$ turbulence model is satisfied. The asymmetric development of the streamwise stress is also here observed due to the same reason discussed in the velocity profiles on the two walls (see Figure 9).
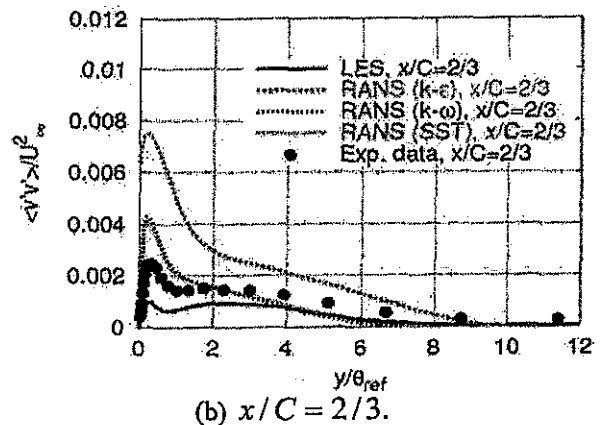


**Figure 11.** Predicted square root of mean-streamwise turbulent stress using SST $k - \omega$ turbulence model against that measured by Webster et al. [2] in the entire domain from the bump surface to the upper wall of the duct at the locations $x/C = 1/2, 2/3, 5/6, 11/12$ and 1 (from left to right).

The computed and the measured wall-normal stress profiles $< v'v' >$ at the same previously discussed locations are presented in Figure 12. It is clear that, LES predictions are in better agreement with the experimental measurements of Webster et al. [2] at

all locations. Except at the locations $x/C = 1/2$ and $2/3$, the computed results from the standard and SST-$k - \omega$ turbulence models show good agreement also. Simultaneously, the standard $k - \varepsilon$ over-predicts the experimental data at all locations. It is interesting to note that in contrast to the streamwise normal stress, the wall-normal stress doesn't exhibit knee points over the summit and downstream of the trailing edge. It is also observed that, the large peak at $x/C = 1$ moves gradually up through the boundary layer with increasing downstream distance and decreases in magnitude. The progress of the peak through the boundary layer is well experimentally and numerically with LES marked by a "hitch" in the $< v'v' >$ profiles, which is first evident nearly at $y/\theta_{ref} = 2$ in the $x/C = 5/6$ profile. This hitch almost appears to pin down the profiles from $x/C = 5/6$ to $x/C = 7/6$, with the region above it almost unaffected by the large peak growing and subsiding below. At $x/C = 4/3$, the inner peak has grown further outward, and the hitch in the profiles is located at approximately $y/\theta_{ref} = 4.5$ and that can be seen experimentally and exact numerically with LES and the standard as well as SST-$k - \omega$ turbulence models, see Figure 12-g.
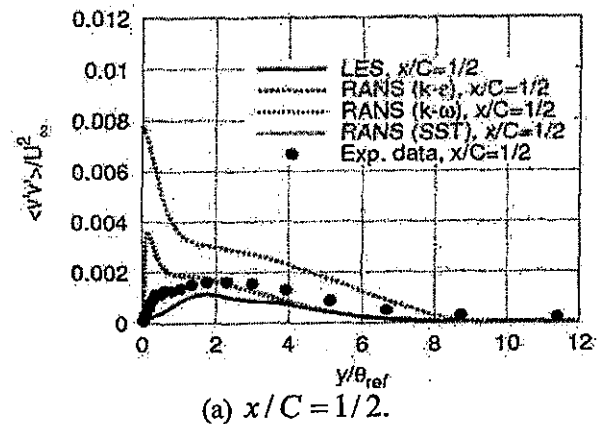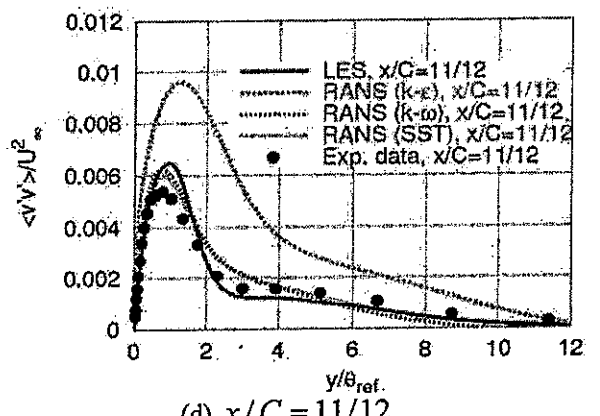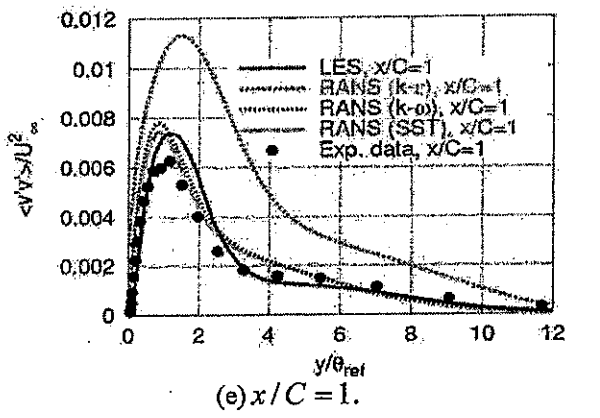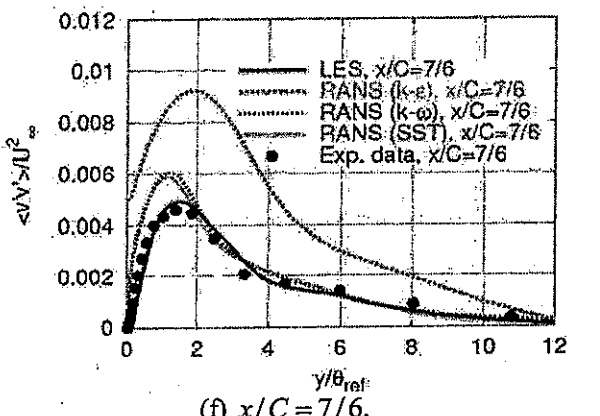


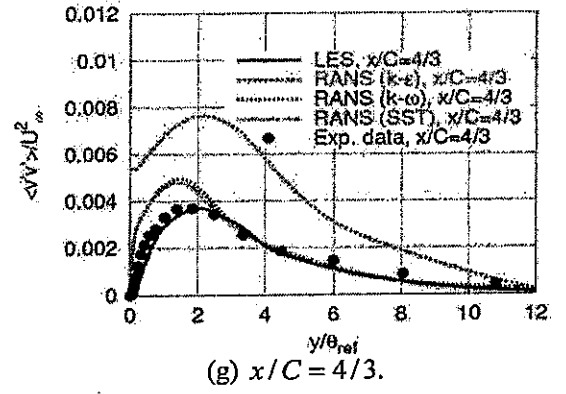(a) $x/C = 1/2$.



(b) $x/C = 2/3$.
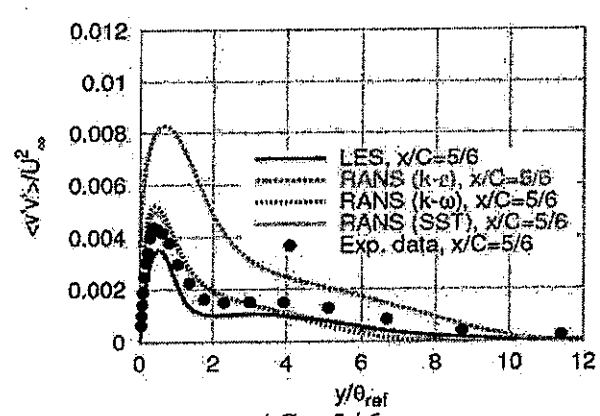
(c) $x/C = 5/6$.



(d) $x/C = 11/12$.



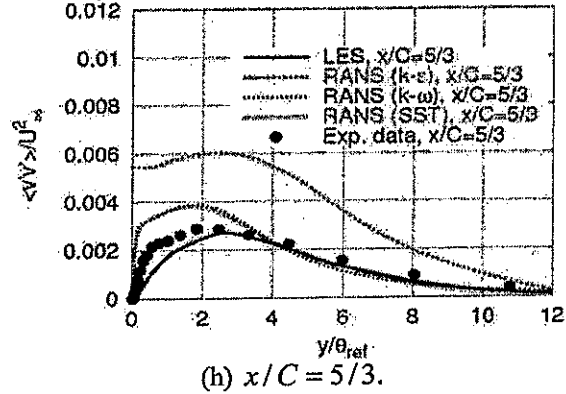(e) $x/C = 1$.



(f) $x/C = 7/6$.



(g) $x/C = 4/3$.



(h) $x/C = 5/3$.

Figure 12. Predicted mean-wall-normal turbulent stress against that measured by Webster et al. [2].

Also the SST $k - \omega$ turbulence model is used to compute the square root of the wall-normal turbulent normal stress as shown in Figure 13. The numerical results is verified with the measured wall-normal stress measured by Webster et al. [2] in the entire domain from the bump surface to the upper wall of the duct at the locations $x/C = 1/2, 2/3, 5/6, 11/12$ and 1. Good comparison of the SST $k - \omega$ turbulence model with the experimental data is clearly noticed.
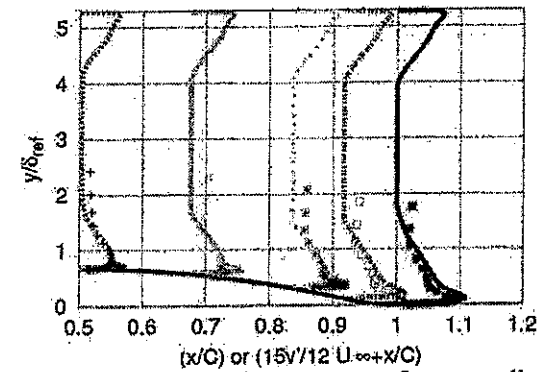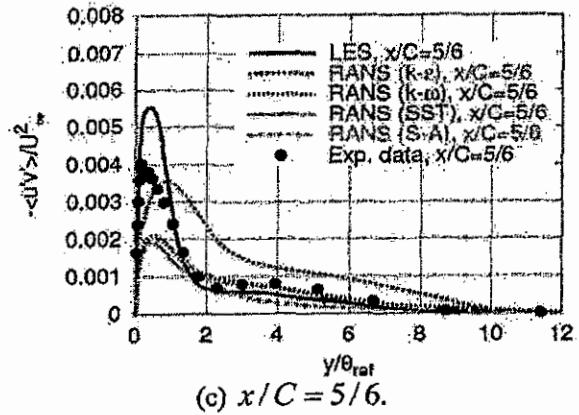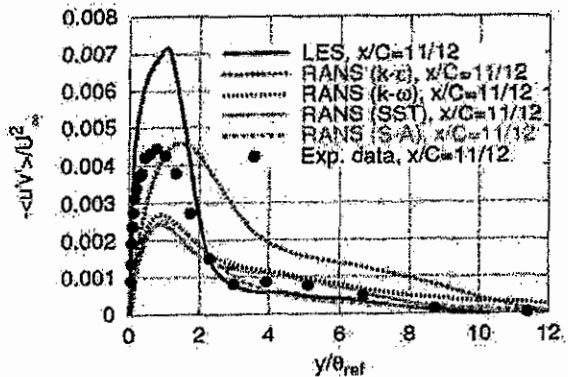


Figure13. Predicted square root of mean-wall-normal turbulent stress using SST $k - \omega$ turbulence model against that measured by Webster et al. [2] in the entire domain from the bump surface to the upper wall of the duct at the locations $x/C = 1/2, 2/3, 5/6, 11/12$ and 1 (from left to right).
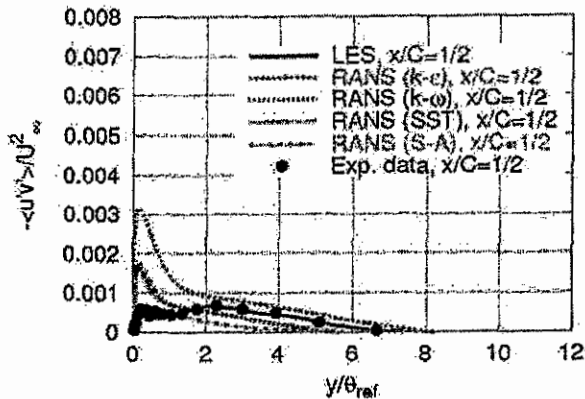
The predicted resolved turbulent shear stress- $<u'v'>$ is compared with that measured by Webster et al. [2] and presented in Figure 14 at all previously discussed locations. The simulations including LES and RANS with all used turbulence models are included. Good agreement of LES results with the experimental data is clearly observed at all locations. At the summit, $x/C = 1/2$, LES predictions of the reduction of shear stress by convex curvature are in reasonably good agreement with the measurements, while clear over-predictions of all used RANS models are noticed. The predictions of LES capture the significant increase in the turbulent shear stress near the wall along the bump surface, where the boundary layer experiences strong adverse pressure gradient, see Figures 14-b to 14-e. All used RANS models, except the standard $k - \varepsilon$ turbulence model, can qualitatively predict the near-wall peaks. As noticed, the standard $k - \varepsilon$ turbulence model over-predicts the peaks at all locations. The over-prediction (especially in the outer region) persists downstream of the trailing edge of the bump. It is noticed that the peak in the turbulent shear stress profiles over the downstream flat plate is a result of the decay of those shown in Figure 14-c, d, which are produced under strong pressure gradient.
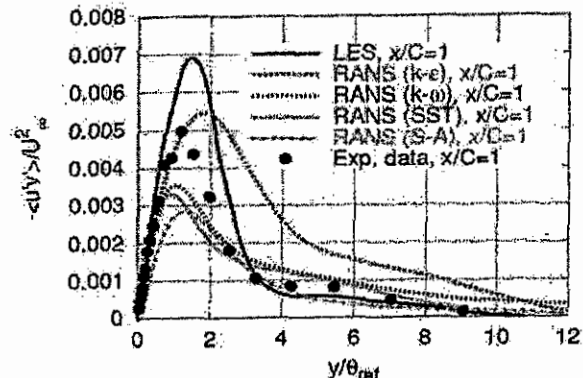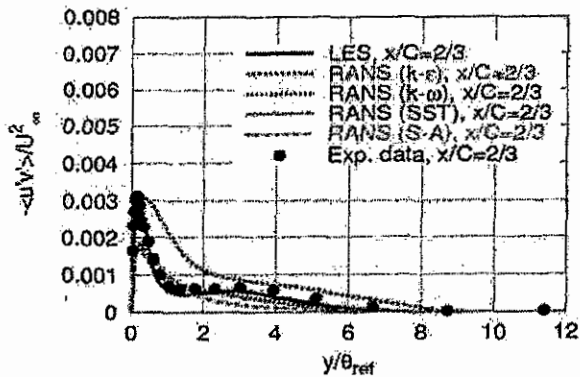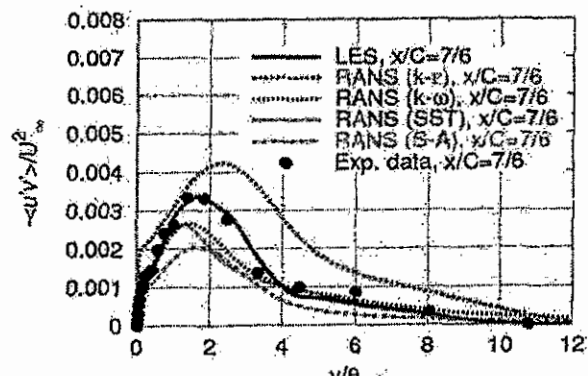

(c) $x/C = 5/6.$


(d) $x/C = 11/12.$


(a) $x/C = 1/2.$


(e) $x/C = 1.$


(b) $x/C = 2/3.$


(f) $x/C = 7/6.$
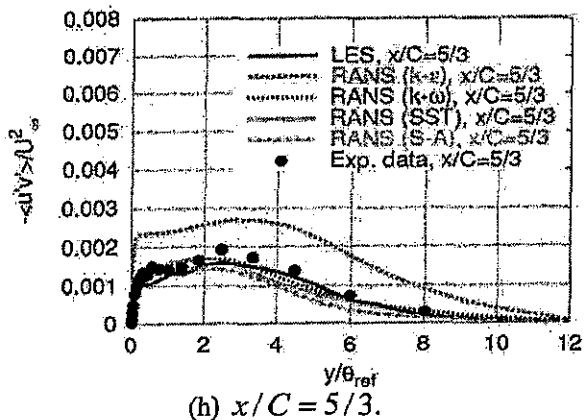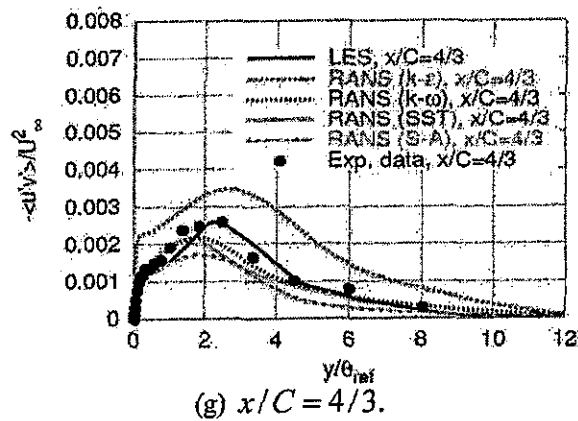
(g) $x/C = 4/3$.



(h) $x/C = 5/3$.

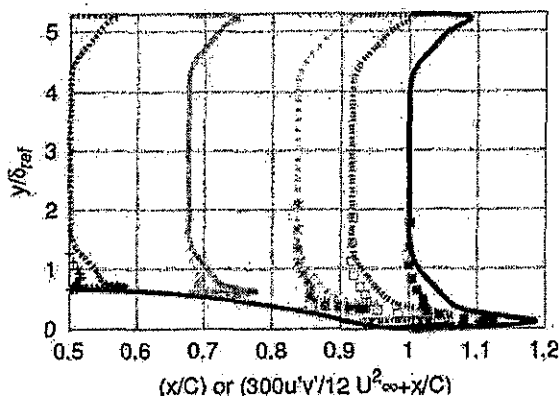**Figure 14.** Predicted turbulent shear stress against that measured by Webster et al. [2].



**Figure 15.** Predicted turbulent shear stress using SST $k - \omega$ turbulence model against that measured by Webster et al. [2] in the entire domain from the bump surface to the upper wall of the duct at the locations $x/C = 1/2, 2/3, 5/6, 11/12$ and 1 (from left to right).

Figure 15 shows comparisons of the measured turbulent shear stress profiles of Webster et al. [2] with the computation of the SST $k - \omega$ turbulence model at locations $x/C = 1/2, 2/3, 5/6, 11/12$ and 1 in the entire duct domain from the bump surface to the upper wall of the duct. The results indicate an enhancement of the turbulent shear stress near the

trailing edge of the bump compared with the other straight upper wall. The concave surface at the trailing edge of the bump is mean reason for this increasing in turbulent shear stress level.

## 5. CONCLUSIONS

A spatially developing turbulent boundary layer flow over a two-dimensional bump has been computed by large-eddy simulation (LES) with dynamic subgrid scale modeling as well as by using the Reynolds-Averaged Navier-Stokes (RANS) equations with various turbulence models. The RANS models include the standard $k - \varepsilon$, the standard $k - \omega$, the shear stress transport (SST) $k - \omega$ as well as the one-equation model or Spalart-Allmaras (S-A) model. The numerical studies are validated with the available experimental data of flow past a two-dimensional bump, in which curvature and pressure-gradient effects are important. A canonical flat plate boundary layer introduced at the inflow boundary to the bump was generated from a separate computation. The flow is then subjected to external perturbations in streamwise pressure gradient and surface curvature and causes a strong departure from equilibrium along the bump surface, relaxing towards equilibrium over the downstream flat plate. The mean velocity is predicted reasonably well by LES and all turbulence models, except in the adverse pressure gradient-region where the LES and the shear stress transport (SST) model predict the mean velocity better than the other tested models.

The interesting feature is that as the flow developed on the downstream side of the bump the boundary layer and an internal layer grew rapidly due the adverse pressure gradient. The knee point in the turbulent stress profiles evolved away from the wall more rapidly than the momentum thickness. The turbulent stresses appeared to be increasing on the downstream side of the bump, but this was due to the internal layer growing away from the wall. In the streamwise turbulent stress profiles, this character is clearly visible from the LES results and qualitatively noticed from SST $k - \omega$ turbulence model. The discontinuity in surface curvature near the trailing edge triggered a second internal layer which is noticed by two maxima in the streamwise turbulent stress profiles. This could be captured using LES with dynamic subgrid scale modeling.

In the adverse pressure-gradient region and in the recovery region of the flow, however, the SST model under-predicts the shear stress by approximately 30%, while the best verification can be obtained from LES in the recovery region. It is found that the RANS models performance is dependent on the flow conditions, whereas the LES performs better than the best studied RANS model (SST $k - \omega$) in the present studied configuration, but with higher

computational costs. On the other hand, the standard $k - \varepsilon$ model needs improvements to capture the streamline curvature.

It is suggested to extend this study, experimentally and numerically, to different bump heights in order to test the quality of turbulence models with the presence of separation. However, the non-linear eddy viscosity is recommended to be used in such configuration. It is also recommended to use the hybrid LES/RANS technique in order to save the computational time.

## 6. REFERENCES

[1] Perry AE and Chong MS. A Description of eddying motions and flow patterns using critical-point concepts. Annual Review of Fluid Mechanics 1987; 19: 125–155.

[2] Webster D, Degraaff D and Eaton JK. Turbulence characteristics of a boundary layer over a two-dimensional bump. Journal of Fluid Mechanics 1996; 320: 53-69.

[3] Wu X and Squires KD. Numerical investigation of the turbulent boundary layer over a bump. Journal of Fluid Mechanics 1998; 362: 229-271.

[4] Germano M, Piomelli U, Moin P and Cabot WH. A Dynamic subgrid-scale eddy viscosity model. Journal of Physics in Fluids 1991; A 3: 1760-1765.

[5] El-Askary WA, Schroeder W and Meinke M. LES of compressible wall-bounded flows. AIAA Paper 2003; 2003-3554.

[6] Verman AW, Geurts BG, Kuerten JGM and Zandbergen PJ. A Finite volume approach to large eddy simulation of compressible, homogeneous, isotropic, decaying turbulence, International Journal for Numerical Methods in Fluids 1992; 15:799-816.

[7] Guo X, Schroeder W and Meinke M. Large eddy simulations of film cooling flows. Journal of Computers & Fluids 2006; 35: 587-606.

[8] Lund TS, Wu X and Squires D. Generation of turbulent inflow data for spatially-developing boundary layer simulations. Journal of Computational Physics 1998; 140: 233-258.

[9] Launder BE and Spalding DB. The numerical computation of turbulent flows. International Journal for Numerical Methods in Fluids 1974; 15:127–46.

[10] Wilcox D. Simulation of transition with a two-equation turbulence model. Journal of AIAA 1994; 32: 1192–1198.

[11] Menter FR. Eddy viscosity transport equations and their relation to the $k - \omega$ model. ASME Journal of Fluids Engineering 1997; 119: 876–884.

[12] Spalart PR and Allmaras SR. A one-equation turbulence model for aerodynamic flows. AIAA Paper 1992: 92-0439.

[13] Yakhot V and Orszag SA. Renormalization group analysis of turbulence: I. Basic theory. Journal of Scientific Computing 1986; 1: 3–51.

[14] Shih TH, Liou WW, Shabbir A, Yang Z and Zhu J. A new $k - \omega$ eddy-viscosity model for high Reynolds number turbulent flows. Journal of Computers & Fluids 1995; 24: 227–238.

[15] Wilcox D. Turbulence modeling for CFD. DCW Industries, second edition 1998.

[16] El-Askary WA and Balabel A. Predictions of reattaching turbulent shear flow in asymmetric divergent channel using linear and non-linear turbulence models. Engineering Research Bulletin 2007, Faculty of Engineering, Menoufiya University; 30, No.4: 535-550.

[17] El-Askary WA and Nasr M. Performance of a bend-diffuser system: experimental and numerical studies, Journal of Computers & Fluids 2009; 38, Issue 1: 160-170.

[18] Patankar SV. Numerical heat transfer and fluid flow. Hemisphere Publishing Corporation 1980.

## 7. NOMENCLATURE

| | |
|---|---|
| C | Bump-chord length |
| $C_f$ | Skin-friction coefficient |
| $C_p$ | Wall-pressure coefficient |
| $C_s$ | Smagorinisky coefficient |
| $D_H$ | Hydraulic diameter |
| H | Height of the wind tunnel |
| h | Bump summit height |
| k | Turbulence kinetic energy |
| $P_k$ | Production of the turbulence kinetic energy |
| $P_\omega$ | Production of the specific dissipation rate |
| p | Pressure |
| Re | REYNOLDS number |
| SST | Shear-stress transport |
| $S_{ij}$ | Strain tensor |
| t | Time |
| $<U>$ | Time-averaged streamwise velocity |
| $U_{bulk}$ | Bulk streamwise velocity |
| $U_\infty$ | Free-stream velocity |
| $u, v, w$ | Unsteady velocity components in a Cartesian system |
| $<u'u'>$, $<v'v'>$, $<u'v'>$ | Streamwise, normal and shear Reynolds stresses, respectively |

$u_\tau$    Friction velocity, $\sqrt{\tau_w / \rho_w}$

$x, y, z$    Coordinates in streamwise, transverse and spanwise direction

$Y_k$    Dissipation of turbulence kinetic energy

$y^+$    Non-dimensional-inner coordinate, $y^+ = u_\tau y / \nu$

$y$    Distance from the wall

**Greek symbols**

$\Delta x^+ \; \Delta y^+ \; \Delta z^+$    Non-dimensional grid spacing in wall coordinate

$\varepsilon$    Turbulence-energy dissipation rate

$\delta$    Boundary layer thickness

$\delta_{ij}$    KRONECKER delta ($\delta_{ij} = 1$ if $i = j$, and $\delta_{ij} = 0$ otherwise)

$\kappa$    VON KÁRMÁN constant ($= 0.41$)

$\mu$    Laminar viscosity

$\mu_t$    Turbulent viscosity

$\nu$    Kinematic viscosity ($= \mu / \rho$)

$\nu_t$    Turbulent kinematic viscosity ($= \mu_t / \rho$)

$\rho$    Fluid density

$\tau_{ij}$    Subgird scale tensor

$\tau_w$    (Time averaged) wall shear stress

$\theta$    Momentum thickness

$\omega$    Specific dissipation rate

**Subscript**

$i, j, k$    Component $i, j, k$ of a vector

$ref$    Reference value

$w$    Wall condition

$\infty$    Free-stream value.

**Acronyms**

AUSM    Advective upstream splitting method

LES    Large-eddy simulation

RANS    Reynolds-Averaged Navier-Stokes

SGS    Sub-grid scale